A *de novo* matrix for macroscopic living materials from bacteria

Authors: Sara Molinari[1], Robert F. Tesoriero Jr.[1,2], Dong Li[3], Swetha Sridhar[1,2], Rong Cai[1], Jayashree Soman[1], Kathleen R. Ryan[4], Paul D. Ashby[3], Caroline M. Ajo-Franklin[1,*]

Affiliations:

1. Department of Biosciences, Rice University, Houston, TX, USA.

2. Systems, Synthetic and Physical Biology PhD program, Rice University, Houston, TX, USA.

3. Molecular Foundry, Lawrence Berkeley National Laboratory, Berkeley, CA, USA.

4. Plant & Microbial Biology, University of California, Berkeley, Berkeley, CA, USA

* corresponding author. Email: cajo-franklin@rice.edu

Abstract:

Engineered living materials (ELMs) embed living cells in a biopolymer matrix to create novel materials with tailored functions. While bottom-up assembly of macroscopic ELMs with a *de novo* matrix would offer the greatest control over material properties, we lack the ability to genetically encode a protein matrix that leads to collective self-organization. Here we report growth of ELMs from *Caulobacter crescentus* cells that display and secrete a self-interacting protein. This protein formed a *de novo* matrix and assembled cells into centimeter-scale ELMs. Discovery of design and assembly principles allowed us to tune the mechanical, catalytic, and morphological properties of these ELMs. This work provides novel tools, design and assembly rules, and a platform for growing ELMs with control over matrix and cellular structure and function.

One-Sentence Summary: We discovered rules to grow bacteria into macroscopic living materials with customizable composition, structure, and function.

Main Text:

Naturally occurring living biomaterials, such as bones or wood, grow bottom-up from a small number of progenitor cells into macroscale structures(*1*). Engineered living materials (ELMs)(*2–4*) are inspired by naturally-occurring living materials, but use synthetic biology to introduce tailored, non-natural functions. By incorporating engineered cells into a biopolymer matrix, these materials can function as living sensors(*5*), therapeutics(*6*, *7*), electronics(*8*), energy converters(*9*), and structural materials(*10*). While cells confer functionality to ELMs, the matrix assembles the material and controls the bulk material composition, structure, and function(*11*). Engineering macroscopic ELMs that grow from the bottom-up with a synthetic matrix remains an unmet challenge. It is considered well beyond the current state-of-the art (*11*)because assembly of micrometer-sized cells into centimeter-scale materials requires self-organization across length scales spanning four orders of magnitude. Engineering principles to achieve this are unknown(*12*), so most ELMs are microscopic(*13–17*). The few macroscopic ELMs have been created by genetically modifying existing matrices(*18*), processing microscopic ELMs into macroscopic ones(*19*, *20*), or incorporating living cells into a chemically synthesized matrix(*6*, *21*). Additionally, secreting biopolymers at high yield is challenging, making synthesis of a *de novo* matrix a technical hurdle(*11*).

Leveraging previous genetic tools for biopolymer secretion and display in *Caulobacter crescentus*(*22*, *23*), we sought to create bottom-up ELMs composed of cells interacting through a surface-bound *de novo* matrix. To minimize native cell-cell interactions, we started with a *C. crescentus* background that cannot form a biofilm. Next, we designed a bottom-up *de novo* (BUD) protein by replacing the native copy of the surface layer (S-layer) RsaA(*24*) (Fig. 1A) with a synthetic construct encoding four modules (Fig. 1B): (i) a surface-anchoring domain, (ii) a flexible biopolymer region for solution accessibility, (iii) a tag for functionalization, and (iv) a domain for secretion and self-interaction. We used the first 250 residues of RsaA as an anchor to the O-antigen lipopolysaccharide(*25*, *26*). As the flexible domain, we chose an elastin-like polypeptide (ELP) based on human tropoelastin with 60 repeats of the Val-Pro-Gly-X-Gly motif(*23*, *27*), ELP_{60}. ELPs are flexible, self-associate, and form elastic structures. SpyTag(*28*) was used as a functionalization tag, as it covalently binds to fusion proteins containing SpyCatcher. The C-terminal domain of the BUD protein, consisting of the last 336 residues of RsaA, was chosen to mediate protein secretion(*23*) and to self-associate(*29*). We refer to this BUD protein-expressing strain of *C. crescentus* as the BUD-ELM strain.

Surprisingly, cultures of the BUD-ELM strain yielded centimeter-scale, filamentous material (Fig. 1C – left) after 24 h of growth. The material contained intact *C. crescentus* cells (Fig. 1C – right), indicating these macroscopic materials were indeed BUD-ELMs. In contrast, the wild-type culture did not generate any visible aggregates (Fig. S1). To understand the role of BUD protein in this material, we compared the extracellular surface of planktonic cells of the BUD-ELM strain before material formation with other *C. crescentus* strains. When stained with SpyCatcher-GFP, cells of the BUD-ELM strain (Fig. 1D – left) showed GFP fluorescence (cyan) along the outer contour of the cells (yellow), demonstrating the BUD protein is on the extracellular surface. The BUD-ELM was not stained by free GFP (Fig. 1D – right), nor was the Δ*SpyTag* strain stained by SpyCatcher-GFP (Fig. S2A,B), confirming that staining required SpyTag and SpyCatcher. Atomic force microscopy (AFM) of the BUD-ELM cells showed a brush-like structure (Fig 1E – right) that distinguished it from the wild-type hexameric S-layer (Fig. 1E – left) and the Δ*rsaA* strain (Fig. 1E – middle). The BUD protein formed long, unstructured projections, and this soft layer mediates cell-cell interactions (Fig. S3). These results provide a first

demonstration of macroscopic, bottom-up ELMs with a *de novo* surface-bound matrix that mediates cell-cell interactions.

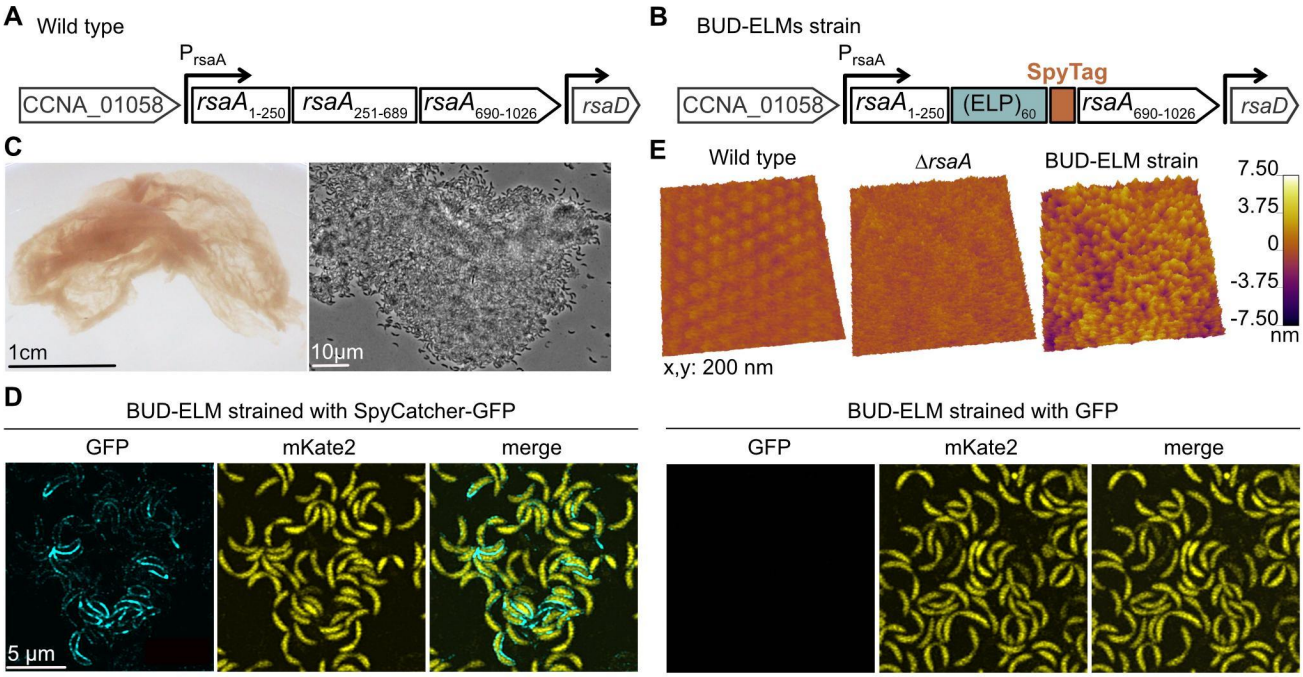

Fig. 1. Engineered strains of *C. crescentus* self-assemble into BUD-ELMs. (**A**) Schematic of the native *rsaA* gene within its genomic context, showing its N-terminal cell anchoring domain (1-250) and C-terminal domain (251-1026) with the secretion subdomain (690-1026). (**B**) Schematic of the four-domain construct replacing the native *rsaA* gene in the BUD-ELM strain. (**C**) Photograph of free-floating material formed by the BUD-ELM strain (left). Brightfield image of a portion of a BUD-ELM (right), showing cell clusters and intact cells. (**D**) Confocal microscopy of single cells of BUD-ELM strain stained with SpyCatcher-GFP (left) or GFP (right), demonstrating that the BUD protein (Fig. 2A, left)n is located on the cell surface. Scale bar: 5 μm, applies to all images. (**E**) AFM images of the cell surface of wild-type (left), Δ*rsaA* (middle), and BUD-ELM strain (right), showing the brush-like structure of the BUD-ELM strain's surface.

To probe their structure, we stained BUD-ELMs with SpyCatcher-GFP and imaged them using confocal microscopy. At the half a millimeter length scale (Fig. 2A – left), the BUD protein (cyan) and cells (yellow) appear distributed throughout the entire material. At the micron length scale, *C. crescentus* cells in the material display a layer of BUD protein (Fig. 2A – right) like planktonic cells (Fig. 1D). At the tens of micron length scale (Fig. 2A – middle), we unexpectedly observed a BUD protein-containing secreted matrix (blue) that was locally inhomogeneous and was surrounded by *C. crescentus* cells (yellow) on all sides (Fig. S4). To probe the matrix composition, we also stained the BUD-ELM with Congo Red and 3,3'-dioctadecyloxacarbocyanine perchlorate (DiO) (Fig. 2B), which are known to bind amyloid proteins(*30*) and lipids(*31*), respectively. Congo Red staining (Fig. 2B – *Proteins*) was orthogonal to the cell channel and analogous to the SpyCatcher-GFP staining, confirming that the matrix is made of proteins. In contrast, DiO (Fig. 2B – *Lipids*), did not stain cell-free regions. Analysis of the cell-free and stained areas (Fig. 2C) confirmed that protein staining had a higher overlap with cell-excluded matrix regions compared to lipid staining. Thus, the BUD-ELM strain produces a secreted proteinaceous matrix containing the BUD protein that mediates BUD-ELM structure at the tens of micron length scale.

To understand how BUD protein could be both a surface-displayed and secreted matrix, we imaged single cells through AFM at early stages of BUD-ELM formation, when cells are mostly in the planktonic state, and at later stages when the material is fully assembled. At the early stage (Fig. 2E – left), the cell surface appeared uniform, but after the BUD-ELM had formed, cells showed large protuberances (Fig. 2E – right). Additionally, the surface layer depth of early-stage BUD-ELM cells is ~10 nm (Fig. 2F – left), compared to the ~35 nm layer of late-stage cells (Fig. 2F – right), indicating that the protein layer thickens over time. We found secreted BUD protein in the medium under both static and shaking conditions (Fig. 2D), indicating that some BUD protein is released into the medium independent of shaking. Moreover, a strain that only secretes, but does not display the BUD protein, created material with a much lower cell content than the BUD-ELM (Fig. S5). These results suggest that the BUD protein accumulates on the cell surface, some of which detaches and forms a secreted matrix that subsequently binds *C. crescentus* cells. We propose that the ability of cells to simultaneously self-interact and adhere to the matrix plays a pivotal role in creating an emergent structure that is cell-rich and macroscopic.

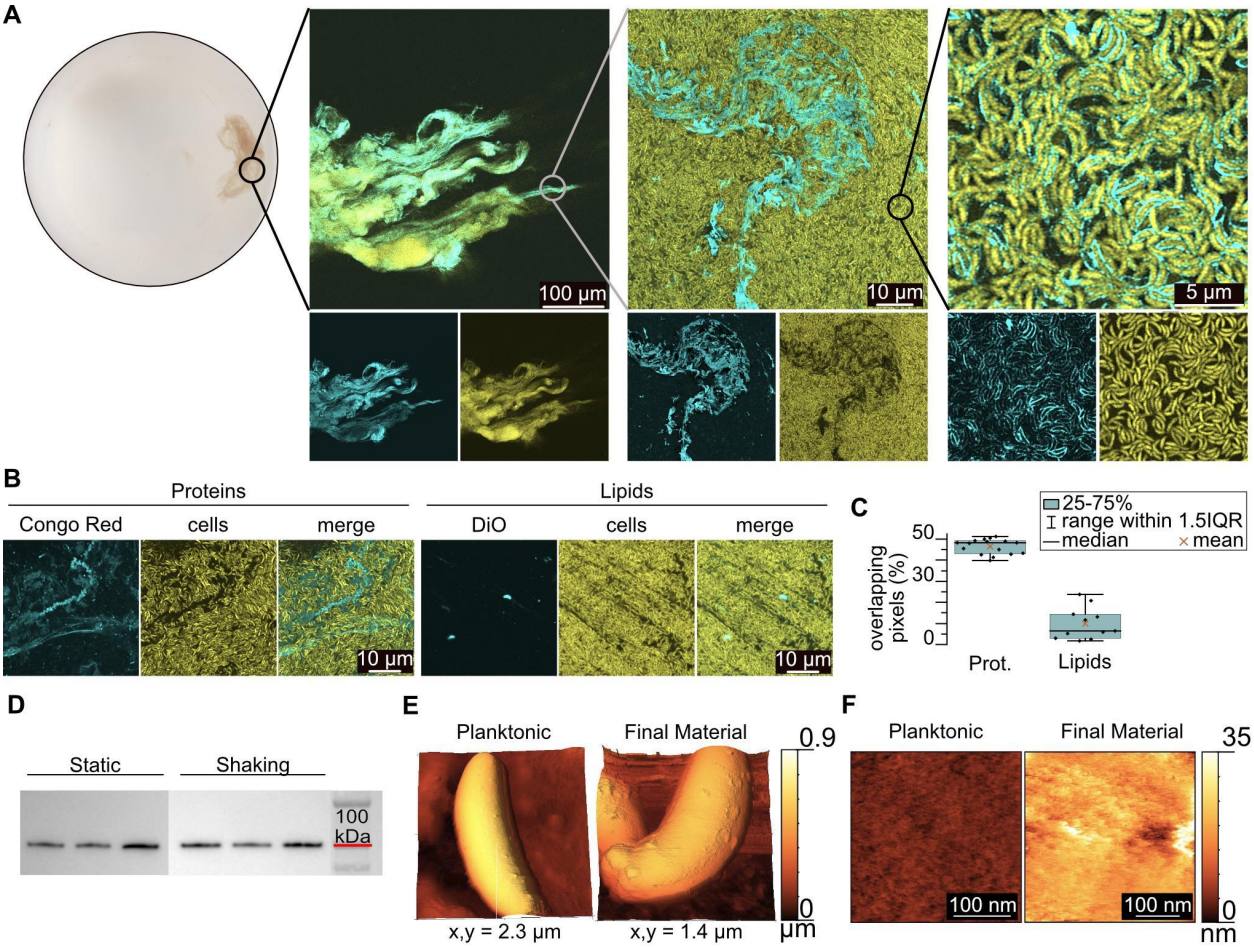

Fig. 2. BUD-ELMs contain a *de novo* protein matrix and display hierarchical structure. (A) Confocal microscopy of ELMs stained with SpyCatcher-GFP at increasing magnifications, showing a hierarchical structure. Bottom images show individual fluorescent channels: GFP (matrix) on the left and mKate2 (cells) on the right. (**B**) Confocal microscopy of BUD-ELMs stained with Congo Red (left panel) and DiO (left panel), highlighting the proteinaceous nature of the BUD protein matrix. (**C**) Percentage of overlapping pixels between cell-free and stained regions, confirming the absence of lipid in the BUD protein matrix.

Error bars represent standard error. (**D**) Immunoblot of BUD protein in growth media in static (left) and shaking (right) cultures. (**E**) AFM images of single cells at early (left) and late (right) stages of BUD-ELM formation, showing a difference in surface morphology. (**F**) High-resolution AFM images of single-cell surfaces at early (left) and late (right) stages of BUD-ELM formation, showing differences in surface layer thickness.

We next sought to understand how this material assembles by imaging BUD-ELM cultures at various times during their growth (Fig. 3A). Shaken cultures grew planktonically for ~ 12 h (Fig. 3A – left) before a thin pellicle appeared at the air-water interface (Fig. 3A – middle). AFM images of the pellicle depicted a central, cell-dense region (Fig. 3B – left) and a peripheral region of a few cells attached to a ~6 nm thick membrane (Fig. 3B – middle and right), suggesting the BUD protein forms a protein membrane to which cells adhere. The pellicle increased in density and opacity, becoming more compact. After ~24 h total culturing time, the pellicle desorbed from the air-water interface and sank as the final material (Fig. 3A – right). Disrupting the hydrophobicity of the air/water interface by the addition of surfactant prevented pellicle and material formation (Fig. S6). Similarly, neither a pellicle nor material formed under static growth conditions. However, when static cultures were shaken, a pellicle formed (Fig. S7). Together, these experiments demonstrate that BUD-ELMs are formed through a multi-step process and establish hydrophobicity of the air/water interface and shaking as critical conditions for assembly of BUD-ELMs.

To understand how physical parameters affect BUD-ELM assembly, we grew cultures under different conditions and measured the size of the resulting materials. The size of BUD-ELMs depended non-monotonically on the shaking speed, volume, and flask diameter (Fig. 3C). We then used these parameters to calculate two quantities: the volumetric power input, P_V, describing the energy provided to the flask by shaking per unit volume and the volumetric mass transfer coefficient, k_{La}, representing the transfer of oxygen into the medium relative to the area of the air-water interface. We found that neither parameter showed a consistent relationship with the size of BUD-ELMs per flask (Fig. S8). Instead, we found empirically that the product of P_V, k_{La}, and the fifth power of the flask diameter, which we refer to as the modified volumetric power parameter, $P_{V,A}$, related the culture conditions to the material size (Fig. 3D). With these data, we propose a model for BUD-ELM assembly (Fig. 3E). During culturing, the BUD protein accumulates in solution and on the surface of *C. crescentus*. With shaking, the BUD protein adsorbs to the air-water interface to form a protein-rich membrane of increasing thickness. BUD protein-displaying cells adhere to the membrane, increasing its density to form a pellicle. Hydrodynamic forces from shaking cause the pellicle to collapse on itself, until the material sinks to the bottom of the flask. At lower $P_{V,A}$ values, the weaker hydrodynamic forces do not collapse the pellicle, and the pellicle fragments into smaller materials. At intermediate $P_{V,A}$ values, stronger hydrodynamic forces collapse the pellicle into a single, large BUD-ELM. At higher $P_{V,A}$ values, shear forces prevent the assembly of larger pellicles, leading to smaller pellicles and final materials. This empirical model provides a basis for the future development of mechanistic models describing BUD-ELM assembly.

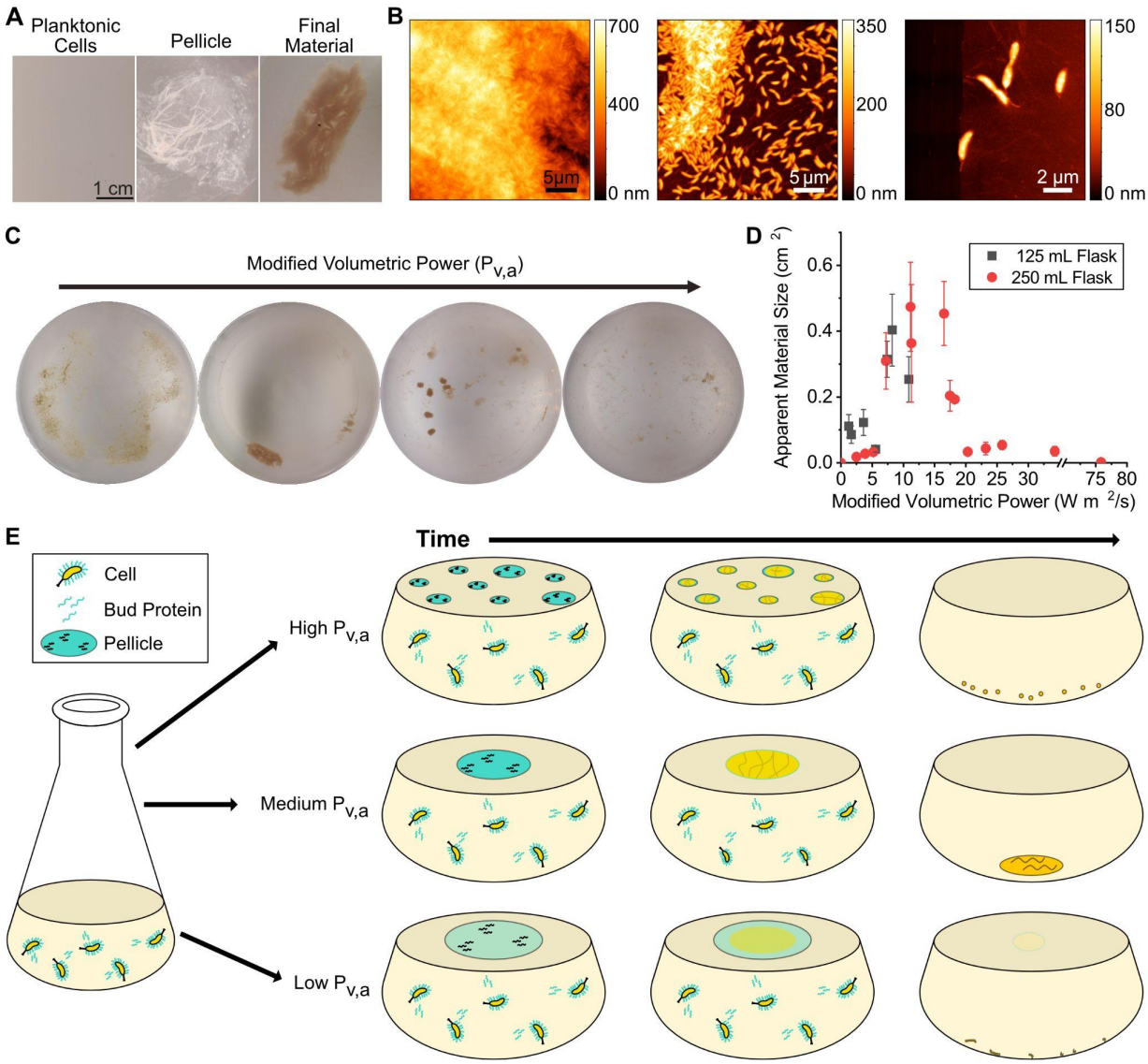

Fig. 3. BUD-ELMs are formed through a shaking-dependent, multi-step process. (**A**) Optical images of representative BUD-ELM strain culture during material, showing BUD-ELMs are formed through a multi-step process. (**B**) AFM images of pellicle structure, showing the pellicle contains both a central region containing several layers of densely packed cells (left), and a peripheral region containing sparse cells connected by a thin membrane (center and right). (**C**) Representative optical images of BUD-ELMs grown under different modified volumetric power values. Altering the modified volumetric power changes the morphology and size of the BUD-ELMs. (**D**) Correlation between modified volumetric power and the apparent surface area of the BUD-ELMs for 125- and 250-mL shake flasks. Error bars represent standard error. (**E**) Proposed mechanism for BUD-ELM formation.

ELMs must be able to be processed and stored without losing their ability to regrow. We dried BUD-ELMs (Fig. 4A – left panel, left and middle image) and re-inoculated fragments of them into fresh medium (Fig. 4A – left panel, right image). BUD-ELM fragments dried for 7, 14, or 21 days regenerated to form additional BUD-ELMs (Fig. 4A, right panel). Whereas BUD-ELMs re-grew 100% of the time after 7 or 14 days of drying, BUD-ELMs desiccated for 21 days regenerated in 33% of cases. Additionally, BUD-ELMs collected from multiple cultures formed a cohesive paste (Fig. 4B – top) that was extrudable through syringes with different diameters (Fig.

4B – bottom left and middle). When mixed with glass powder, BUD-ELMs created a firmer paste that hardened into a solid composite (Fig. 4B – bottom, right image). These results indicate that BUD-ELMs can regenerate after drying, can be reshaped, and can be processed into composite materials.

Next, we used our understanding of design and assembly rules to reprogram the matrix and BUD-ELM properties. First, we removed the flexible ELP_{60} domain from the Δ*SpyTag* strain (Fig. 4C – left panel). The ΔELP_{60}Δ*SpyTag* strain produced a less compact and less cohesive BUD-ELM than the original strain (Fig. 4C – right panel), demonstrating that we can control the material characteristics genetically. Second, hypothesizing that nutrients would affect BUD-ELM assembly, we added different sugars to the growth media. Addition of glucose and sucrose favored the formation of smaller aggregates (Fig. 4D). In contrast, xylose, under specific growth conditions (Fig. S9), had a dramatic effect on ELM morphology, inducing the formation of extended, cord-like structures (Fig. 4E – right panel, middle and bottom). These cords could be stretched several times their original length (Supplementary Movie 1), demonstrating high elasticity. Both the elasticity of this material and the observation that the ΔELP_{60}Δ*SpyTag* BUD-ELM grown in the same conditions did not show any changes in morphology or elasticity (Fig. S10) indicates that ELP plays a critical role in this structure. While more investigation is necessary to elucidate the mechanisms that drive changes in BUD-ELMs, these results show that altering the modular structure of BUD protein and the growth conditions can change the bulk properties of BUD-ELMs.

Lastly, we probed the ability of BUD-ELMs to behave as functional materials. Self-regenerating materials that remove heavy metals from water could help address the growing prevalence of heavy metal contamination. Since many forms of biomass non-specifically absorb heavy metals, we hypothesized that the BUD-ELM could remove Cd^{2+} from solution. When 0.013±0.007g of Δ*SpyTag* BUD-ELM was incubated for 90 min with a $CdCl_2$ solution of 6 ppb–1 ppb above the Environmental Protection Agency (EPA) limit–90 ±5 % of cadmium was removed (Fig. 4F). Next, we functionalized the BUD-ELM matrix to allow it to perform biological catalysis. We fused the oxidoreductase PQQ-glucose dehydrogenase (GDH), which couples oxidation of glucose to reduction of a soluble electron carrier(*32*), to SpyCatcher. Cell lysates containing over-expressed *apo* SpyCatcher-GDH or GDH were reconstituted by adding the cofactor PQQ (pyrroloquinoline quinone) to obtain the *holo* forms of the enzyme. After confirming the activity of *holo* GDH in both cases, we observed that only BUD-ELMs incubated with SpyCatcher-*holo*-GDH enzymatically reduced an electron carrier (Fig. 4G and Fig. S12A). This demonstrates that BUD-ELM can be functionalized directly from complex mixtures to act as catalysts. Together, these results show BUD-ELMs can serve as versatile functional materials.

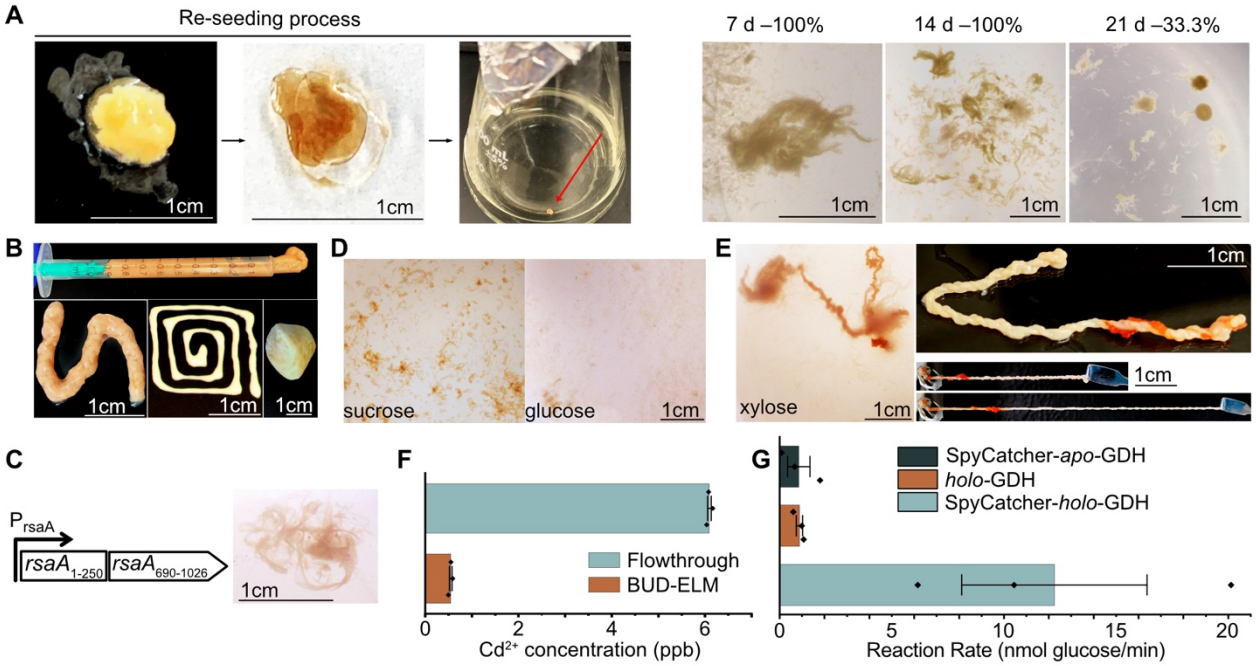

Fig. 4. BUD-ELMs are self-regenerating, processible, and functional materials. (**A**) Representative example of BUD-ELMs reseeding (left montage), showing extraction from liquid culture (left), desiccated (middle) and inoculation into fresh medium (right). Representative example of BUD-ELMs grown from desiccated material (right montage) after 7 (left), 14 (middle) or 21 (right) days. The percentage of successful BUD-ELM regeneration was 100%, 100% and 33.3% respectively. (**B**) BUD-ELMs collected into a syringe (top) for extrusion using different-sized nozzles, (bottom-left and bottom-middle), showing their ability to be reshaped. BUD-ELMs mixed with glass powder to form a firm paste that hardens when dehydrated (bottom-right), showing its potential as cement-like agent. (**C**) Genetic constructs replacing the native *rsaA* gene in the Δ*ELP*$_{60}$Δ*SpyTag* (left), and image of corresponding BUD-ELM (right). (**D**) BUD-ELMs grown with sucrose (left) or glucose (right), showing the formation of small cell aggregates. (**E**) BUD-ELMs grown with xylose (left). The isolated cord-like structure (top-right) exhibits an elastic behavior (middle and bottom-right). (**F**) Graph showing the final Cd^{2+} solution concentration after 6 ppb Cd^{2+} solution was incubated with (BUD-ELM) or without (flowthrough) the Δ*SpyTag* BUD-ELMs. Error bars represent standard error (**G**) Graph showing the rate of glucose oxidation for BUD-ELMs that were incubated with SpyCatcher-*holo*-GDH, *holo*-GDH, or SpyCatcher-*apo*-GDH. Error bars represent standard error.

In this work, the serendipitous creation of macroscopic ELMs allowed us to identify a new design principle - that macroscale BUD-ELMs are associated with a secreted extracellular matrix. We suggest that cell-matrix interactions may be essential for BUD-ELMs to reach a macroscopic size. This idea is supported by previous literature that shows that neither cell-cell adhesion alone(*16*), nor sparse cell-matrix interactions in the absence of additional forces(*33*) lead to microscopic cell aggregates. Additionally, we have demonstrated that nucleation of a pellicle at the liquid-air interface and hydrodynamically-driven coalescence and collapse of the pellicle are required to form macroscopic ELMs. Since pellicle formation is also a key step in nanocellulose-based living materials(*18*), we suggest that the use of the air-water interface to locally concentrate and order hydrophobic biomolecules into a matrix may represent a general assembly principle for macroscopic ELMs. The new tools and *C. crescentus* platform developed here will permit systematic exploration of design and assembly rules for programming the growth of centimeter-scale structures using living cells as building blocks.

By creating BUD-ELMs with a *de novo*, modular protein matrix, this work greatly expands the ability to tailor macroscopic ELMs for specific applications. Existing examples of macroscopic, bottom-up ELMs have extracellular matrices predominantly composed of polysaccharides, allowing little composition control(*18*). The modularity of the BUD protein and the ease of engineering protein biopolymers offer much greater opportunities for introducing desirable properties into the matrix(*11*). Known polypeptides and proteins can exhibit desirable optical, electrical, mechanical, thermal, transport, and catalytic properties(*34*). We envision specific matrix properties that can be combined synergistically with existing cellular functions such as sensing, biomolecule production, and information processing. Thus, this work multiplies the opportunities to program ELMs tailored for applications in human health, energy, and the environment.

References:

1. U. G. K. Wegst, H. Bai, E. Saiz, A. P. Tomsia, R. O. Ritchie, Bioinspired structural materials. *Nature Materials*. **14**, 23–36 (2015).

2. P. Q. Nguyen, N. M. D. Courchesne, A. Duraj-Thatte, P. Praveschotinunt, N. S. Joshi, Engineered Living Materials: Prospects and Challenges for Using Biological Systems to Direct the Assembly of Smart Materials. *Advanced Materials*. **30**, 1704847–1704847 (2018).

3. W. V. Srubar, Engineered Living Materials: Taxonomies and Emerging Trends. *Trends in Biotechnology*. **39**, 574–583 (2021).

4. T.-C. Tang, B. An, Y. Huang, S. Vasikaran, Y. Wang, X. Jiang, T. K. Lu, C. Zhong, Materials design by synthetic biology. *Nature Reviews Materials*, 1–19 (2020).

5. X. Liu, H. Yuk, S. Lin, G. A. Parada, T.-C. Tang, E. Tham, C. de la Fuente-Nunez, T. K. Lu, X. Zhao, 3D Printing of Living Responsive Materials and Devices. *Advanced Materials*. **30**, 1704821 (2018).

6. L. M. González, N. Mukhitov, C. A. Voigt, Resilient living materials built by printing bacterial spores. *Nature Chemical Biology*. **16**, 126–133 (2020).

7. J. J. Hay, A. Rodrigo-Navarro, K. Hassi, V. Moulisova, M. J. Dalby, M. Salmeron-Sanchez, Living biointerfaces based on non-pathogenic bacteria support stem cell differentiation. *Sci Rep*. **6**, 21809 (2016).

8. K. Krawczyk, S. Xue, P. Buchmann, G. Charpin-El-Hamri, P. Saxena, M.-D. Hussherr, J. Shao, H. Ye, M. Xie, M. Fussenegger, Electrogenetic cellular insulin release for real-time glycemic control in type 1 diabetic mice. *Science*. **368**, 993–1001 (2020).

9. Y.-C. Yong, Y.-Y. Yu, X. Zhang, H. Song, Highly Active Bidirectional Electron Transfer by a Self-Assembled Electroactive Reduced-Graphene-Oxide-Hybridized Biofilm. *Angewandte Chemie International Edition*. **53**, 4480–4483 (2014).

10. W. Pungrasmi, J. Intarasoontron, P. Jongvivatsakul, S. Likitlersuang, Evaluation of Microencapsulation Techniques for MICP Bacterial Spores Applied in Self-Healing Concrete. *Sci Rep*. **9**, 12484 (2019).

11. S. Molinari, R. F. Tesoriero, C. M. Ajo-Franklin, Bottom-up approaches to engineered living materials: Challenges and future directions. *Matter*. **4**, 3095–3120 (2021).

12. C. Gilbert, T. Ellis, Biological Engineered Living Materials: Growing Functional Materials with Genetically Programmable Properties. *ACS Synth. Biol.* **8**, 1–15 (2019).

13. H. Wang, Z. Wang, G. Liu, X. Cheng, Z. Chi, C. Madzak, C. Liu, Z. Chi, Genetical Surface Display of Silicatein on Yarrowia lipolytica Confers Living and Renewable Biosilica–Yeast Hybrid Materials. *ACS Omega*. **5**, 7555–7566 (2020).

14. P. Q. Nguyen, Z. Botyanszki, P. K. R. Tay, N. S. Joshi, Programmable biofilm-based materials from engineered curli nanofibres. *Nature Communications*. **5**, 4945 (2014).

15. A. Y. Chen, Z. Deng, A. N. Billings, U. O. S. Seker, M. Y. Lu, R. J. Citorik, B. Zakeri, T. K. Lu, Synthesis and patterning of tunable multiscale materials with engineered cells. *Nature Mater*. **13**, 515–523 (2014).

16. D. S. Glass, I. H. Riedel-Kruse, A Synthetic Bacterial Cell-Cell Adhesion Toolbox for Programming Multicellular Morphologies and Patterns. *Cell*. **174**, 649-658.e16 (2018).

17. Y. Wang, B. An, B. Xue, J. Pu, X. Zhang, Y. Huang, Y. Yu, Y. Cao, C. Zhong, Living materials fabricated via gradient mineralization of light-inducible biofilms. *Nat Chem Biol*. **17**, 351–359 (2021).

18. C. Gilbert, T.-C. Tang, W. Ott, B. A. Dorr, W. M. Shaw, G. L. Sun, T. K. Lu, T. Ellis, Living materials with programmable functionalities grown from engineered microbial co-cultures. *Nature Materials*, 1–10 (2021).

19. A. M. Duraj-Thatte, A. Manjula-Basavanna, N.-M. D. Courchesne, G. I. Cannici, A. Sánchez-Ferrer, B. P. Frank, L. van't Hag, S. K. Cotts, D. H. Fairbrother, R. Mezzenga, N. S. Joshi, Water-processable, biodegradable and coatable aquaplastic from engineered biofilms. *Nat Chem Biol*. **17**, 732–738 (2021).

20. N.-M. Dorval Courchesne, A. Duraj-Thatte, P. K. R. Tay, P. Q. Nguyen, N. S. Joshi, Scalable Production of Genetically Engineered Nanofibrous Macroscopic Materials via Filtration. *ACS Biomater. Sci. Eng.* **3**, 733–741 (2017).

21. P. Q. Nguyen, L. R. Soenksen, N. M. Donghia, N. M. Angenent-Mari, H. de Puig, A. Huang, R. Lee, S. Slomovic, T. Galbersanini, G. Lansberry, H. M. Sallum, E. M. Zhao, J. B. Niemi, J. J. Collins, Wearable materials with embedded synthetic biology sensors for biomolecule detection. *Nat Biotechnol*, 1–9 (2021).

22. M. Charrier, D. Li, V. R. Mann, L. Yun, S. Jani, B. Rad, B. E. Cohen, P. D. Ashby, K. R. Ryan, C. M. Ajo-Franklin, Engineering the S-Layer of Caulobacter crescentus as a

Foundation for Stable, High-Density, 2D Living Materials. *ACS Synthetic Biology*. **8**, 181–190 (2019).

23. M. T. Orozco-Hidalgo, M. Charrier, N. Tjahjono, R. F. Tesoriero, D. Li, S. Molinari, K. R. Ryan, P. D. Ashby, B. Rad, C. M. Ajo-Franklin, Engineering High-Yield Biopolymer Secretion Creates an Extracellular Protein Matrix for Living Materials. *mSystems*. **6**, e00903-20.

24. T. A. M. Bharat, D. Kureisaite-Ciziene, G. G. Hardy, E. W. Yu, J. M. Devant, W. J. H. Hagen, Y. V. Brun, J. A. G. Briggs, J. Löwe, Structure of the hexagonal surface layer on Caulobacter crescentus cells. *Nature Microbiology*. **2**, 1–6 (2017).

25. S. G. Walker, D. N. Karunaratne, N. Ravenscroft, J. Smit, Characterization of mutants of Caulobacter crescentus defective in surface attachment of the paracrystalline surface layer. *Journal of Bacteriology*. **176**, 6312–6323 (1994).

26. A. von Kügelgen, H. Tang, G. G. Hardy, D. Kureisaite-Ciziene, Y. V. Brun, P. J. Stansfeld, C. V. Robinson, T. A. M. Bharat, In Situ Structure of an Intact Lipopolysaccharide-Bound Bacterial Surface Layer. *Cell*. **180**, 348-358.e15 (2020).

27. S. Roberts, M. Dzuricky, A. Chilkoti, Elastin-like polypeptides as models of intrinsically disordered proteins. *FEBS Letters*. **589**, 2477–2486 (2015).

28. B. Zakeri, J. O. Fierer, E. Celik, E. C. Chittock, U. Schwarz-Linek, V. T. Moy, M. Howarth, Peptide tag forming a rapid covalent bond to a protein, through engineering a bacterial adhesin. *PNAS*. **109**, E690–E697 (2012).

29. W. H. Bingle, J. F. Nomellini, J. Smit, Secretion of the Caulobacter crescentusS-Layer Protein: Further Localization of the C-Terminal Secretion Signal and Its Use for Secretion of Recombinant Proteins. *Journal of Bacteriology*. **182**, 3298–3301 (2000).

30. E. I. Yakupova, L. G. Bobyleva, I. M. Vikhlyantsev, A. G. Bobylev, Congo Red and amyloids: history and relationship. *Bioscience Reports*. **39**, BSR20181415 (2019).

31. A. Majewska, G. Yiu, R. Yuste, A custom-made two-photon microscope and deconvolution system. *Pflügers Arch - Eur J Physiol*. **441**, 398–408 (2000).

32. F. Lisdat, PQQ-GDH – Structure, function and application in bioelectrochemistry. *Bioelectrochemistry*. **134**, 107496 (2020).

33. Engineering Bacillus subtilis for the formation of a durable living biocomposite material | bioRxiv, (available at https://www.biorxiv.org/content/10.1101/2021.08.13.456252v1).

34. D. Kaplan, K. McGrath, *Protein-Based Materials* (Springer Science & Business Media, 1997).

35. J. Büchs, U. Maier, C. Milbradt, B. Zoels, Power consumption in shaking flasks on rotary shaking machines: II. Nondimensional description of specific power consumption and flow

regimes in unbaffled flasks at elevated liquid viscosity. *Biotechnology and Bioengineering*. **68**, 594–601 (2000).

36. W. Klöckner, J. Büchs, Advances in shaking technologies. *Trends in Biotechnology*. **30**, 307–314 (2012).

37. A. J. J. Olsthoorn, J. A. Duine, Production, Characterization, and Reconstitution of Recombinant Quinoprotein Glucose Dehydrogenase (Soluble Type; EC 1.1.99.17) Apoenzyme ofAcinetobacter calcoaceticus. *Archives of Biochemistry and Biophysics*. **336**, 42–48 (1996).

38. A. Persat, H. A. Stone, Z. Gitai, The curved shape of Caulobacter crescentus enhances surface colonization in flow. *Nat Commun*. **5**, 3824 (2014).

Acknowledgements: We thank Marimikel Charrier, Maria Orozco Hidalgo, and Dr. Vera Troselj for helpful conversations.

Funding: This work was primarily supported by the Defense Advanced Research Projects Agency (Engineered Living Materials Program, C.M.A-F.). Additional support was provided by Cancer Prevention and Research Institute of Texas (RR190063, C.M.A-F.) and Office of Naval Research (N00014-21-1-2362, C.M.A-F.). Work at the Molecular Foundry was supported by the Office of Science, Office of Basic Energy Sciences, of the U.S. Department of Energy under Contract No. DE-AC02-05CH11231.

Author contributions:

Conceptualization: SM, RFT, DL, CAF, KRR, PDA

Methodology: SM, RFT, RC, SS, JS, DL, CAF

Investigation: SM, RFT, RC, SS, JS, DL

Visualization: SM, RFT, RC, DL

Funding acquisition: CAF, KRR, PDA

Project administration: CAF

Supervision: SM, CAF

Writing – original draft: SM, CAF, RFT

Writing – review & editing: SM, CAF, RFT, RC, SS, JS, DL, KRR, PDA

Competing interests: The authors declare no competing interests.

Data and materials availability: All strains and plasmids can be supplied upon reasonable request.

Supplementary Materials

Materials and Methods

Supplementary Text

Figs. S1 to S12

Tables S1 to S3

References (*35*–*38*)

Movies S1